

# Electronic Supplementary Information for “Applying molecular simulation to the analysis of lipid monolayer reflectometry”

A. R. McCluskey,<sup>1,2,\*</sup> J. Grant,<sup>3</sup> A. J. Smith,<sup>2</sup> J. L. Rawle,<sup>2</sup> D. J. Barlow,<sup>4</sup> M. J. Lawrence,<sup>5</sup> S. C. Parker,<sup>1</sup> and K. J. Edler<sup>1,†</sup>

<sup>1</sup>*Department of Chemistry, University of Bath, Claverton Down, Bath, BA2 7AY, UK*

<sup>2</sup>*Diamond Light Source, Harwell Campus, Didcot, OX11 0DE, UK*

<sup>3</sup>*Computing Services, University of Bath, Claverton Down, Bath, BA2 7AY, UK*

<sup>4</sup>*Institute of Pharmaceutical Science, King’s College London, London, SE1 9NH, UK*

<sup>5</sup>*Division of Pharmacy and Optometry, University of Manchester, Manchester, M13 9PT, UK*

(Dated: January 15, 2019)

---

\* a.r.mccluskey@bath.ac.uk

† k.edler@bath.ac.uk

## S1. ABELÈS MATRIX FORMALISM

The Abelès matrix formalism method invoked the use of the chemically-consistent monolayer model. For this it is necessary to have the scattering length of the individual head and tail components of the different lipid contrasts, these are given in Table SI.

TABLE SI. The different scattering lengths of the head and tail lipid components.

Contrast	d <sub>13</sub> -DSPC	d <sub>70</sub> -DSPC	d <sub>83</sub> -DSPC	h-DSPC
b <sub>head</sub> 10 × 10 <sup>-4</sup> Å	19.54	11.21	24.75	6.01
b <sub>tail</sub> 10 × 10 <sup>-4</sup> Å	-3.58	69.32	69.32	-3.58

In order to apply the Abelès matrix formalism, the SLD for the layers,  $N$ , were determined as detailed in the text of the paper. This SLD <sub>$N$</sub>  allows for the determination of the wavevector,  $k_N$  at a particular  $q$ -vector in the  $N$ -th layer, by considering the difference in SLD between the layer  $N$  and the semi-infinite layer 0 (Figure 1),

$$k_N^2 = k_0^2 - 4\pi(\text{SLD}_N - \text{SLD}_0) \quad (\text{S1})$$

where  $k_0 = q/2$  and SLD<sub>0</sub> is the SLD of the superphase. For each of the interfaces between two layers, it is possible to evaluate a Fresnel coefficient,  $r_{N,N+1}$ , which describes the refraction of the probing radiation occurring between the layers  $N$  and  $N + 1$ ,

$$r_{N,N+1} = \frac{k_N - k_{N+1}}{k_N + k_{N+1}} \exp(-2k_N k_{N+1} \sigma_{N,N+1}^2). \quad (\text{S2})$$

The exponential factor is due to the fact that the layer is unlikely to be perfectly smooth and will therefore have some roughness, this is modelled as an error function with some width  $\sigma_{N,N+1}$  [1]. A phase factor,  $\beta_N$ , which considers the layer thickness,  $d_N$ , and the wavevector can then be found,

$$\beta_N = \begin{cases} 0 + 0i & N = 0, \\ k_N d_N & N > 0. \end{cases} \quad (\text{S3})$$

These two parameters are then brought together in the characteristic matrix for the layer,  $C_N$ ,

$$C_N = \begin{bmatrix} \exp \beta_N & r_{N,N+1} \exp \beta_N \\ r_{N,N+1} \exp -\beta_N & \exp -\beta_N \end{bmatrix}, \quad (\text{S4})$$

the product sum of which gives a resultant matrix for each value of  $q$ ,

$$M(q) = \prod_{n=0}^{n_{\max}} C_N. \quad (\text{S5})$$

From this matrix, the reflected intensity,  $R(q)$ , can be determined,

$$R(q) = \frac{|M(q)_{21}|}{|M(q)_{11}|}. \quad (\text{S6})$$

## S2. MARTINI POTENTIAL MODEL CONSIDERATIONS

It was noted in the work of Koutsoubas [2], that the use of the MARTINI water bead, could result in the ordering of the water structure. This can be observed in the scattering length density profile (Figure S1) when the layer thickness of 1 Å was used. In an effort to reduce this effect, a larger layer thickness, or 4 Å was used for the MARTINI potential model.

A negative effect of this large layer thickness, was that the smoothness associated with the 1 Å layer was lost. In an effort to reproduce this, an interfacial roughness of 0.8 Å (20 % of the layer thickness) was included in the model. We believe that this gave the MARTINI potential model a fair chance to reproduce the experimental data. However, as is noted in the main text of the paper, the systematic beading problem lead to more severe issues.

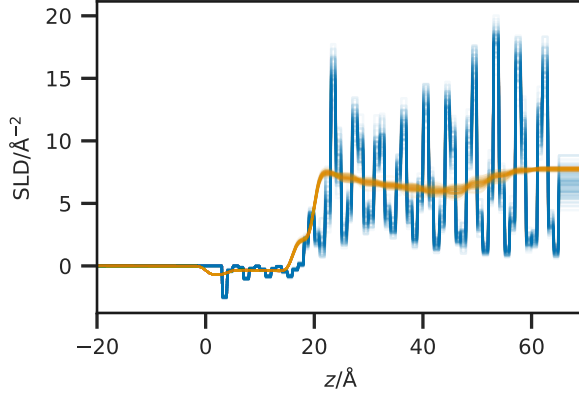


FIG. S1. The scattering length density profile from the MARTINI simulation, at an effective surface pressure of  $30\text{ mN m}^{-1}$  with a layer thickness of  $1\text{ \AA}$  (blue) and  $4\text{ \AA}$  (orange).

### S3. REFLECTOMETRY PROFILES

Figures S2 through S4 show the reflectometry profiles for each of the analysis methods that correspond to surface pressures of  $20\text{ mN m}^{-1}$ ,  $40\text{ mN m}^{-1}$ , and  $50\text{ mN m}^{-1}$ . The profile that corresponds to a surface pressure of  $30\text{ mN m}^{-1}$  is given in Figure 4.

### S4. PROBABILITY DISTRIBUTION FUNCTIONS

Figures S5 to S16 show the probability distribution functions for each of the four parametric outcomes from the simulations.

- [1] L. Nérot and P. Croce, Rev. Phys. Appl. (Paris) **15**, 761 (1980).
- [2] A. Koutsoubas, J. Phys. Chem. B **120**, 11474 (2016).

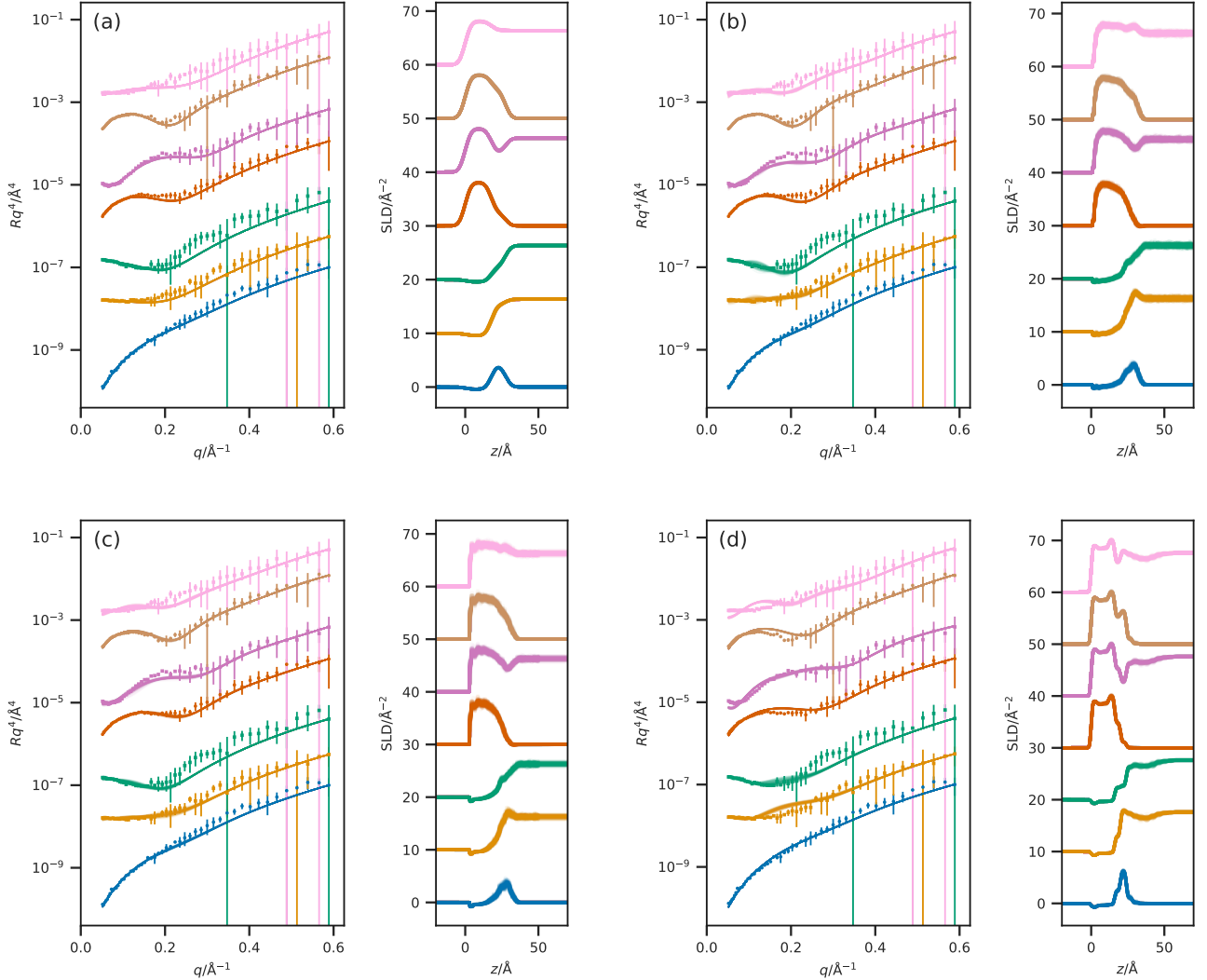


FIG. S2. A comparison of the reflectometry and SLD profiles obtained from (a) the monolayer model, (b) the Slipid simulation, (c) the Berger force-force simulation, and (d) the MARTINI potential model simulation at a surface pressure of  $20 \text{ mN m}^{-1}$ . From top-to-bottom the contrasts are as follows;  $d_{83}\text{-D}_2\text{O}$ ,  $d_{83}\text{-ACMW}$ ,  $d_{70}\text{-D}_2\text{O}$ ,  $d_{70}\text{-ACMW}$ ,  $\text{h-D}_2\text{O}$ ,  $d_{13}\text{-D}_2\text{O}$ ,  $d_{13}\text{-ACMW}$ . The different contrast reflectometry profiles have been offset in the  $y$ -axis by an order of magnitude and the SLD profiles offset in the  $y$ -axis by  $1 \times 10^{-6} \text{ \AA}^{-2}$ , for clarity.

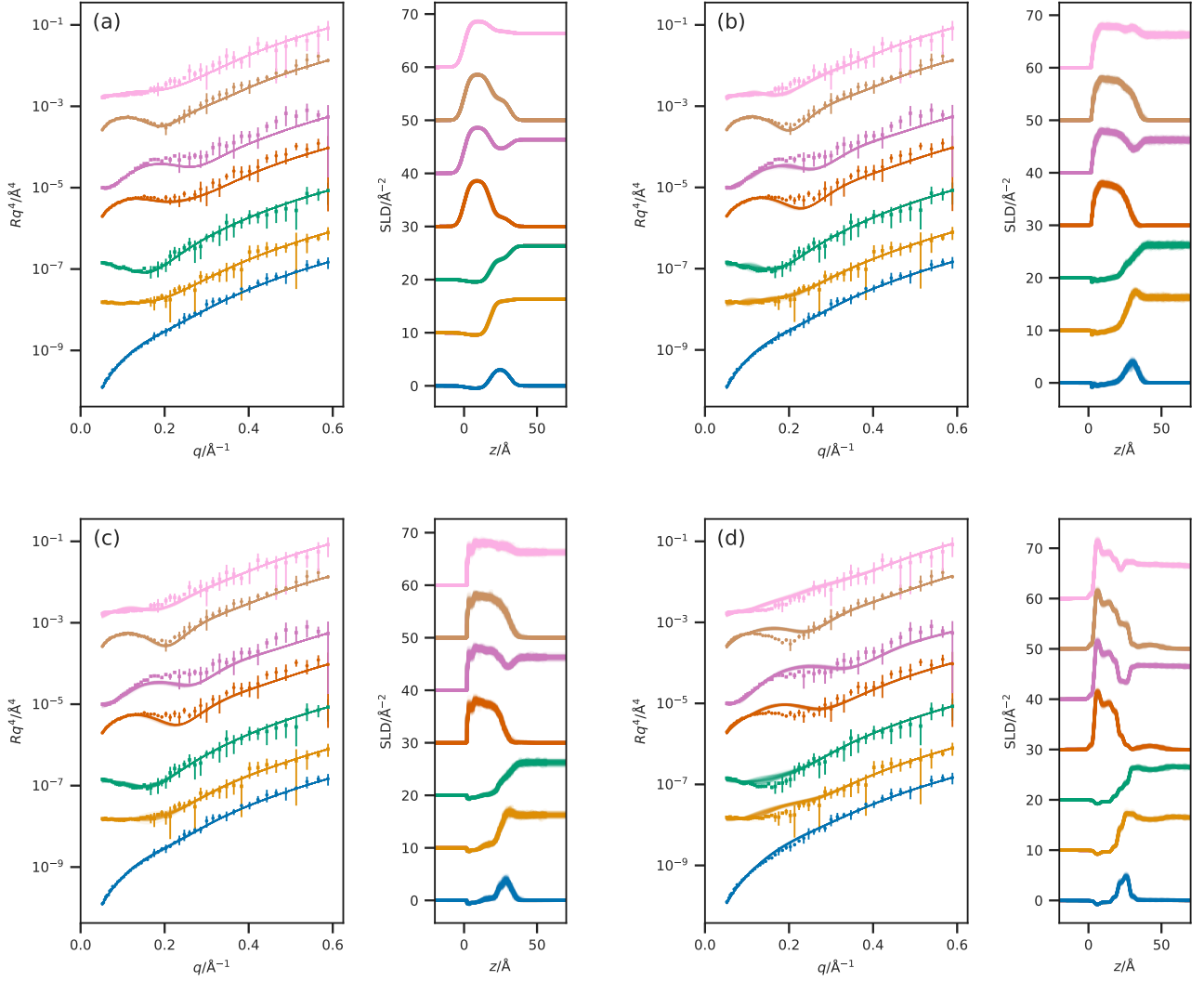


FIG. S3. A comparison of the reflectometry and SLD profiles obtained from (a) the monolayer model, (b) the Slipid simulation, (c) the Berger force-force simulation, and (d) the MARTINI potential model simulation at a surface pressure of  $40 \text{ mN m}^{-1}$ . From top-to-bottom the contrasts are as follows;  $d_{83}-\text{D}_2\text{O}$ ,  $d_{83}-\text{ACMW}$ ,  $d_{70}-\text{D}_2\text{O}$ ,  $d_{70}-\text{ACMW}$ ,  $\text{h-D}_2\text{O}$ ,  $d_{13}-\text{D}_2\text{O}$ ,  $d_{13}-\text{ACMW}$ . The different contrast reflectometry profiles have been offset in the  $y$ -axis by an order of magnitude and the SLD profiles offset in the  $y$ -axis by  $1 \times 10^{-6} \text{ \AA}^{-2}$ , for clarity.

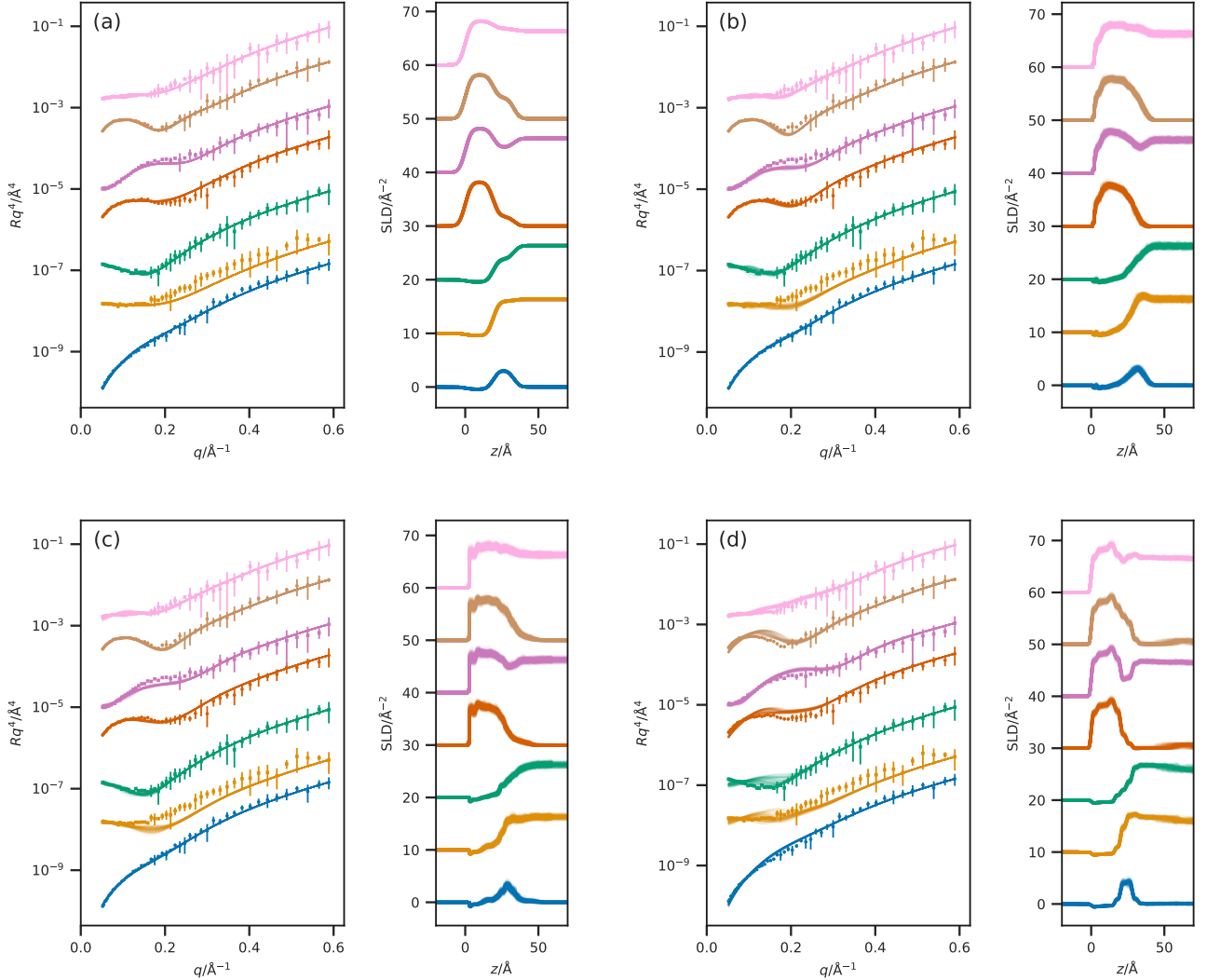


FIG. S4. A comparison of the reflectometry and SLD profiles obtained from (a) the monolayer model, (b) the Slipid simulation, (c) the Berger force-force simulation, and (d) the MARTINI potential model simulation at a surface pressure of  $50 \text{ mN m}^{-1}$ . From top-to-bottom the contrasts are as follows;  $d_{83}-\text{D}_2\text{O}$ ,  $d_{83}-\text{ACMW}$ ,  $d_{70}-\text{D}_2\text{O}$ ,  $d_{70}-\text{ACMW}$ ,  $\text{h}-\text{D}_2\text{O}$ ,  $d_{13}-\text{D}_2\text{O}$ ,  $d_{13}-\text{ACMW}$ . The different contrast reflectometry profiles have been offset in the  $y$ -axis by an order of magnitude and the SLD profiles offset in the  $y$ -axis by  $1 \times 10^{-6} \text{ Å}^{-2}$ , for clarity.

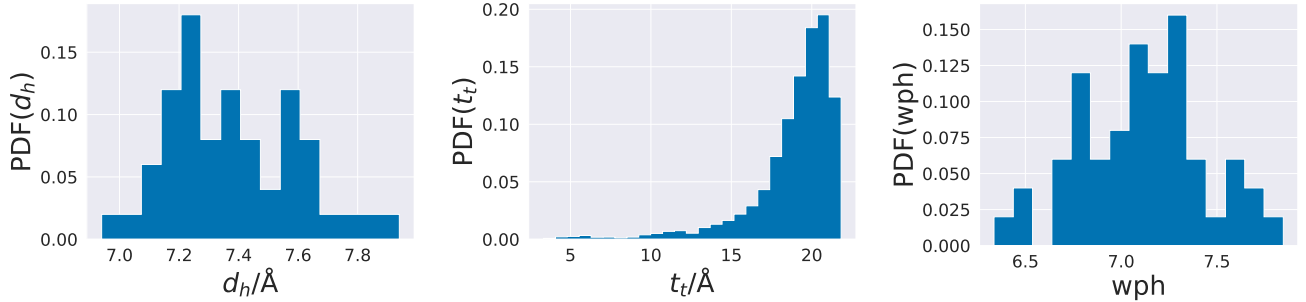


FIG. S5. The probability distribution functions for each of the parametric outcomes from the Slipid potential model simulation with a effective surface pressure of  $20 \text{ mN m}^{-1}$ .

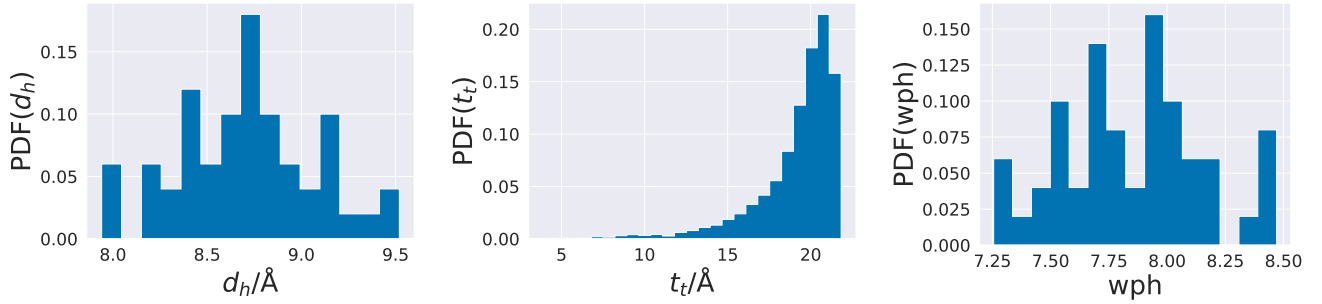


FIG. S6. The probability distribution functions for each of the parametric outcomes from the Slipid potential model simulation with a effective surface pressure of  $30 \text{ mN m}^{-1}$ .

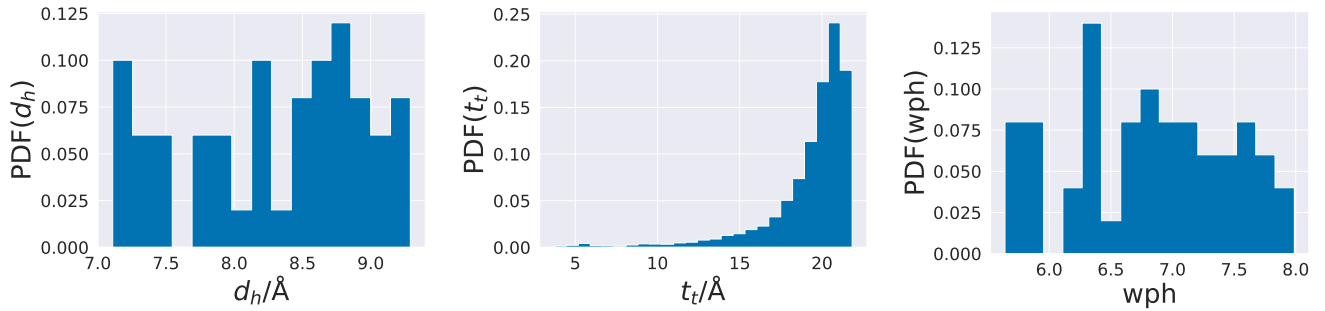


FIG. S7. The probability distribution functions for each of the parametric outcomes from the Slipid potential model simulation with a effective surface pressure of  $40 \text{ mN m}^{-1}$ .

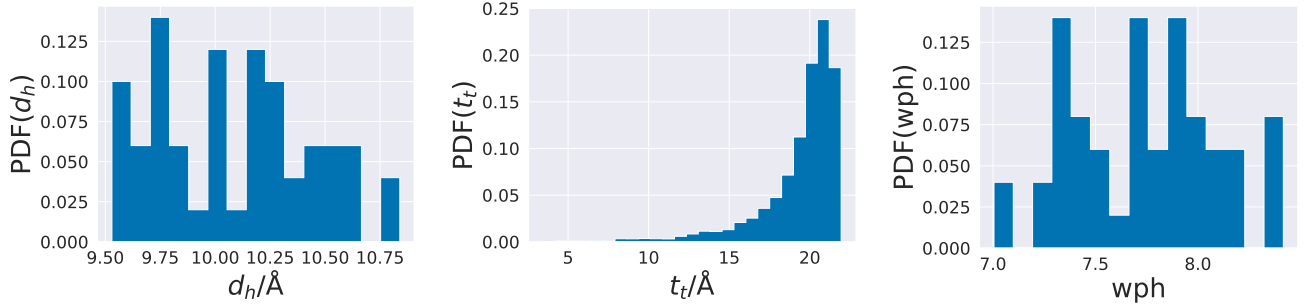


FIG. S8. The probability distribution functions for each of the parametric outcomes from the Slipid potential model simulation with a effective surface pressure of  $50 \text{ mN m}^{-1}$ .

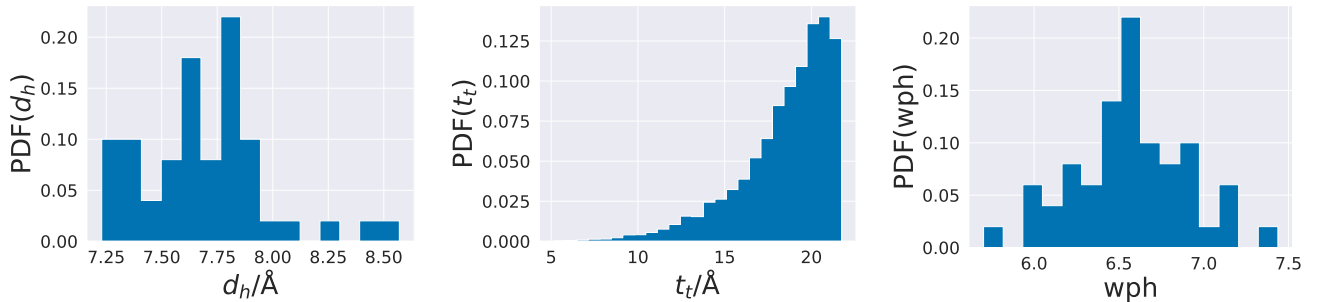


FIG. S9. The probability distribution functions for each of the parametric outcomes from the Berger potential model simulation with a effective surface pressure of  $20 \text{ mN m}^{-1}$ .

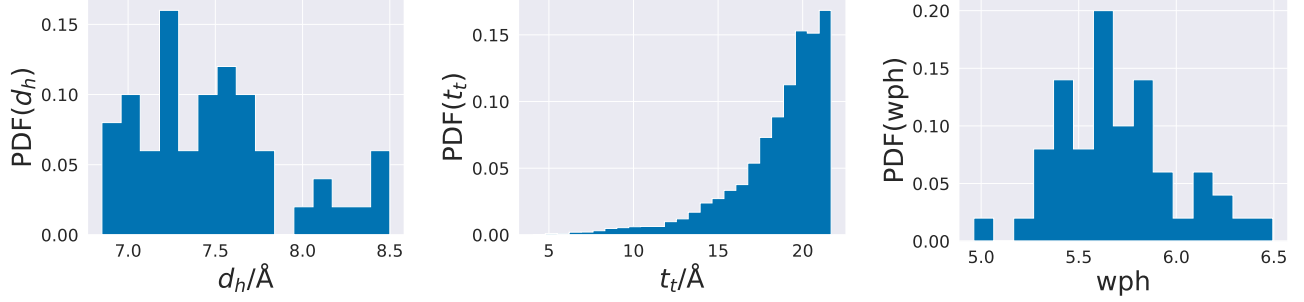


FIG. S10. The probability distribution functions for each of the parametric outcomes from the Berger potential model simulation with an effective surface pressure of  $30 \text{ mN m}^{-1}$ .

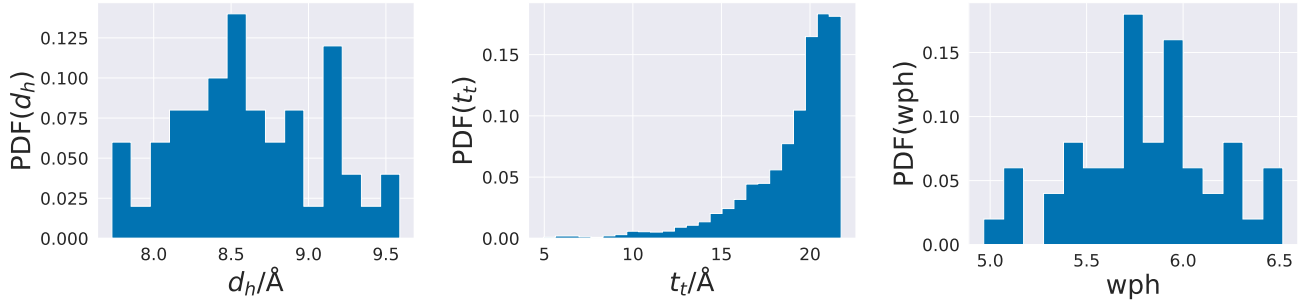


FIG. S11. The probability distribution functions for each of the parametric outcomes from the Berger potential model simulation with an effective surface pressure of  $40 \text{ mN m}^{-1}$ .

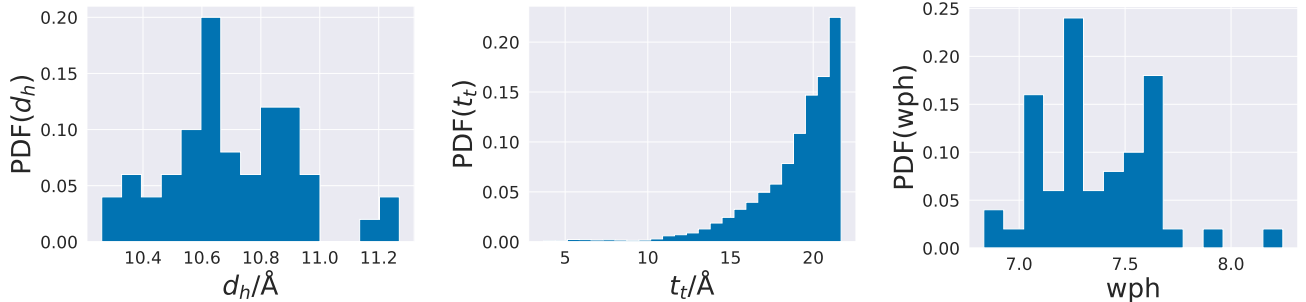


FIG. S12. The probability distribution functions for each of the parametric outcomes from the Berger potential model simulation with an effective surface pressure of  $50 \text{ mN m}^{-1}$ .

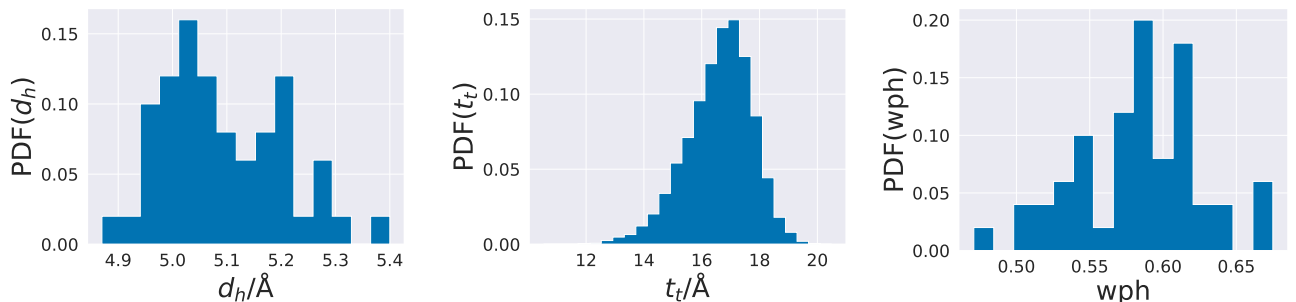


FIG. S13. The probability distribution functions for each of the parametric outcomes from the MARTINI potential model simulation with an effective surface pressure of  $20 \text{ mN m}^{-1}$ .

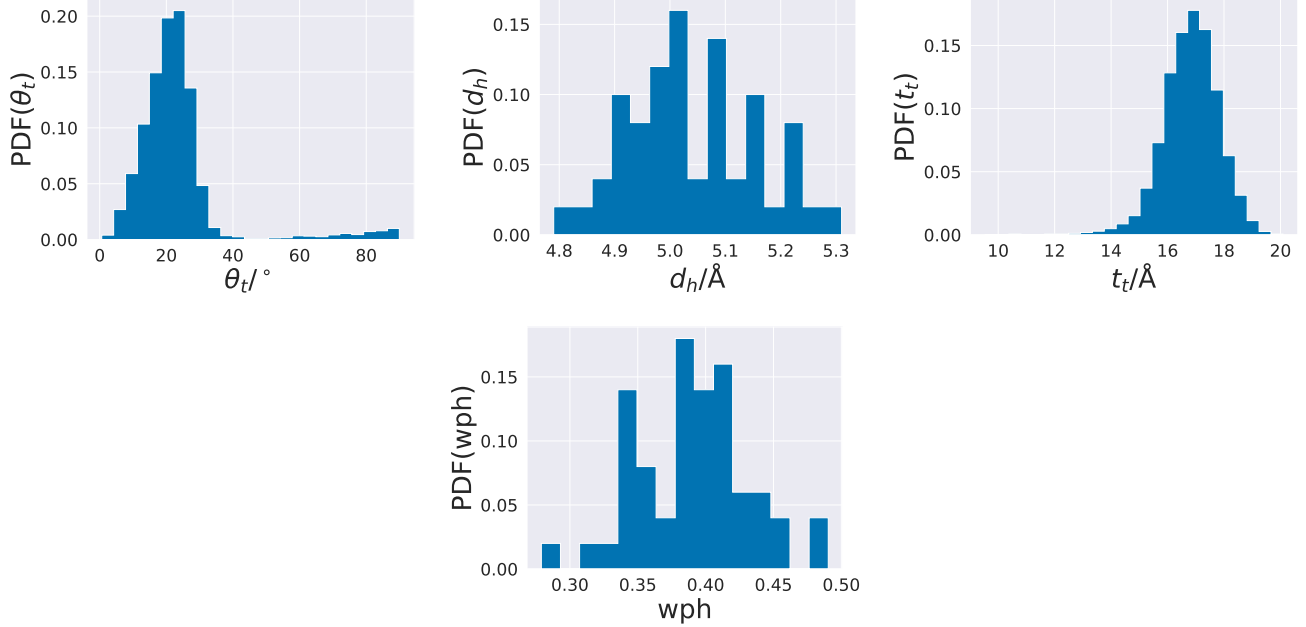


FIG. S14. The probability distribution functions for each of the parametric outcomes from the MARTINI potential model simulation with a effective surface pressure of  $30 \text{ mN m}^{-1}$ .

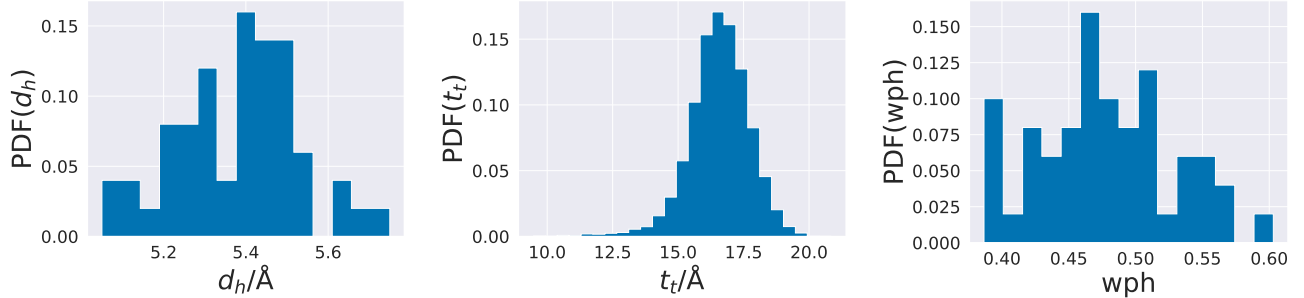


FIG. S15. The probability distribution functions for each of the parametric outcomes from the MARTINI potential model simulation with a effective surface pressure of  $40 \text{ mN m}^{-1}$ .

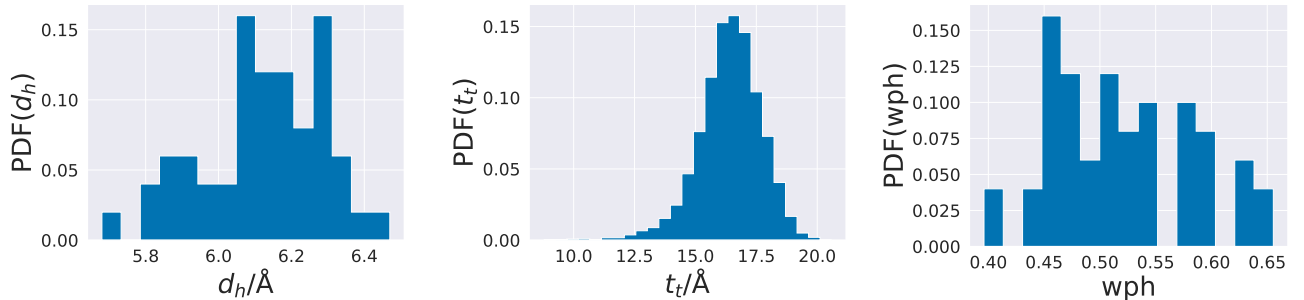


FIG. S16. The probability distribution functions for each of the parametric outcomes from the MARTINI potential model simulation with a effective surface pressure of  $50 \text{ mN m}^{-1}$ .